Dynamics of a Serpentine Diffuser with a Cowl Inlet

Travis J. Burrows,[1] Bojan Vukasinovic[2] and Ari Glezer[3]
Georgia Institute of Technology, Atlanta, Georgia, 30332-0405

The flow within a serrated cowl inlet of a serpentine diffuser is investigated experimentally with emphasis on the formation and evolution of streamwise vortices and their effects on the flow dynamics. The time-resolved flow structure is studied using stereo PIV measurements, spectral total pressure analysis at the aerodynamic interface plane (AIP), and surface oil-flow visualization. The present investigations show that the flow is dominated by two pairs of counter-rotating streamwise vortices that are formed along the edges of the serrated cowl lip and result in significant pressure losses and flow distortion. The interactions of these vortices with the internal flow are mitigated by exploiting auxiliary bleed flow that is driven by pressure differences across the cowl's shell through an array of narrow spanwise slots. Simultaneous reduction in the fraction of the flow drawn through the cowl face and displacement of the weakened vortices away from the inner surfaces, along with the small-scale mixing promoted by the bleed flow through the slots, result in broad band attenuation of pressure fluctuations and pressure losses across the AIP that are associated with 35% reduction in peak instantaneous circumferential distortion.

Nomenclature

AIP	aerodynamic interface plane
D	diffuser AIP diameter
$DPCP$	SAE circumferential distortion descriptor
$DPCP_{avg}$	average SAE circumferential distortion descriptor
f	frequency
H	diffuser inlet height
L	diffuser length
M_{AIP}	AIP Mach number
PR	pressure recovery
p_t	total pressure
q	turbulent kinetic energy
U	streamwise velocity component
W	diffuser throat width
Γ	circulation
ω_x	streamwise vorticity component

I. Introduction

Inlet systems of future fighter aircraft will use embedded engines and more compact, three-dimensionally offset inlet-airframe integration to attain a small spot factor and aerodynamic efficiency. Such inlet systems utilize complex serpentine diffusers that present flow-management challenges, effected by the development of large-scale vortices and boundary-layer separation coupled to throat shocks and aggressive diffuser turns. This secondary-flow phenomenon results in reduced total-pressure recovery and increased flow distortion at the engine face, which can be detrimental to engine operability and performance, but could be mitigated with the implementation of flow-control technology.

Poor performance of supersonic inlets in low-speed conditions has been a known issue for decades. Henne [1] pointed out that a high-speed cruise requires thin inlet lips to keep the inlet mass flow ratio high and to minimize the nacelle size and, therefore, keep drag as small as possible. However, high performance at low-speed conditions, such as zero forward speed with crosswind and low forward speed with high angle of attack, requires thick inlet lips to

[1] Graduate Research Assistant, AIAA Member.
[2] Research Engineer, AIAA Member.
[3] Professor, AIAA Fellow.

ingest the outer flow without separation. The effect of a sharp lip in low-speed air flow was theoretically characterized by Fradenburgh and Wyatt [2] using momentum balance analysis on a cylindrical inlet at subsonic free-stream Mach numbers. With this analysis they estimated total-pressure recovery as a function of freestream and inlet Mach numbers. At lower freestream Mach numbers, and especially in the case of zero freestream Mach number, the total pressure recovery plummets, greatly reducing aircraft engine performance. A supersonic inlet model was tested experimentally and found results in reasonable agreement to the theory. Lower pressure recovery means that if an aircraft needs to operate at that condition, it will need a larger engine, increasing the weight and size of the aircraft.

Aircraft that require high performance in both low-speed and high-speed conditions need a variable geometry inlet. The vertical and/or short take-off and landing (V/STOL) fighter type aircraft were among the first to encounter this issue, because they must both hover (high inlet speed, zero free-stream Mach number) and cruise at a high speed. In the 1960s, during the development of the prototype Hawker P1127 V/STOL aircraft, an inflatable lip was designed and tested [3]. The idea was to inflate a rubber balloon on the lip to approximate a bell-mouth during low-speed operation and deflate it to create a sharp lip for high-speed operation. After testing, this solution was determined to be not feasible because the rubber would ripple and tear at high speeds.

The 'auxiliary' inlet with passive flaps known as blow-in doors were ultimately chosen and implemented on Harrier production aircraft [4]. An auxiliary inlet is a bell-mouth-like slot going around the circumference of the primary inlet that increases the inlet area and enables some mass flow to bypass the sharp lip leading to higher pressure recovery. The blow-in doors are hinged covers for the slots that open when the pressure is lower within the inlet (at low-speed operation) and remain shut when the opposite is true (at high-speed operation). Similar blow-in covers for low-speed operation were used on the Boeing 707, 737-200, and 747, on the B-52, and MiG-29 [5], and to provide extra stall margin during takeoff and landing on General Dynamics' YF-16 [6]. Powell et al. [7] conducted tests of variable cowl slots on an axisymmetric mixed-compression supersonic inlet in 1985 at free stream Mach numbers of 0, 0.1, and 0.2. They reported that at low speeds the slot reduced flow separation associated with the sharp lip as well as improve the total pressure recovery and time-averaged distortion. Garzon [8] used CFD simulations to investigate the benefits of integrating a translating cowl on a supersonic business jet to improve low speed performance at free stream Mach number of 0.1 and reported that while the pressure recovery was improved, pressure distortion increased and was attributed to the positioning of the boundary-layer diverter, which changed the pattern of incoming flow.

The present work focuses on the flow dynamics in a serpentine diffuser integrated with a cowl inlet that is designed for high-speed flight, during low-speed (takeoff) operation. Thin cowl profiles, designed for supersonic speeds hinder efficient intake of low-speed air without separation, as the inlet acts as a sink under static or near-static conditions, and air drawn from all directions cannot efficiently make sharp turns around the cowl lip. Specific attention is paid to the cowl-induced streamwise vortices whose unsteady interactions dominate the flow within the diffuser and lead to time variations in total pressure sectional distributions. The present experimental investigation is concerned with such a low-radius-of-curvature cowl geometry at zero free-stream Mach number (static condition), with an objective of characterization of the base flow dynamics and contrasting it to the analogous 'isolated' diffuser dynamics. Lastly, since Burrows et al. [9] already showed that autonomous bleed flow control across a cowl can overcome detrimental effects of the cowl at the take-off and landing conditions, the current work assesses the changes in the diffuser flow dynamics in the presence of jets of air that is drawn by the pressure differences across the cowl.

II. Experimental Setup and Flow Diagnostics

The present experiments are performed in an open-return, pull-down, high-speed subsonic wind tunnel driven by a 150 hp blower in which the temperature of the return air is controlled using a chiller, coupled with an ultra-low pressure drop heat exchanger (Figure 1). An aggressive offset diffuser model having a cowl inlet (Figure 2a) is installed in the tunnel and a ground plane at the cowl's inlet emulates the effect of an adjacent aerodynamic surface. It is noted that in the present experiments, the diffuser geometry is identical to the one that was previously integrated into a wind tunnel [10], where the square outlet of the tunnel contraction is connected to the diffuser's D-shape inlet through an adapter section (Figure 2b). The cowl inlet and ground plane replace the 106:1 area-ratio contraction to better approximate the flow in a diffuser with an inlet that is integrated

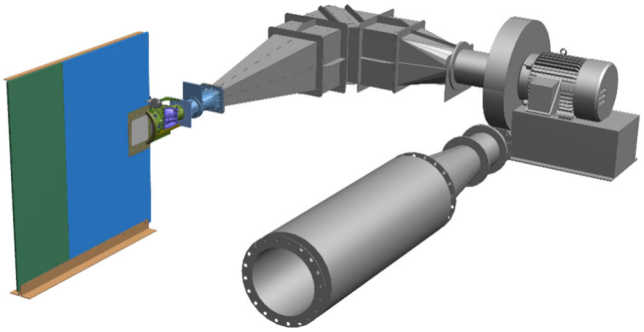

Figure 1. *CAD model of pull-down wind tunnel facility with a flat-plate approach-flow geometry.*

onto an aircraft wing. Downstream of the cowl, the diffuser has a *D*-shaped inlet and a round aerodynamic interface plane (AIP) with diameter, $D = D_{AIP} = 0.127$ m. The offset between the throat and AIP is $0.4 \cdot D$, length-to-diameter ratio $L/D = 3.7$, throat width $W/D = 1.78$, and height $H/D = 0.48$.

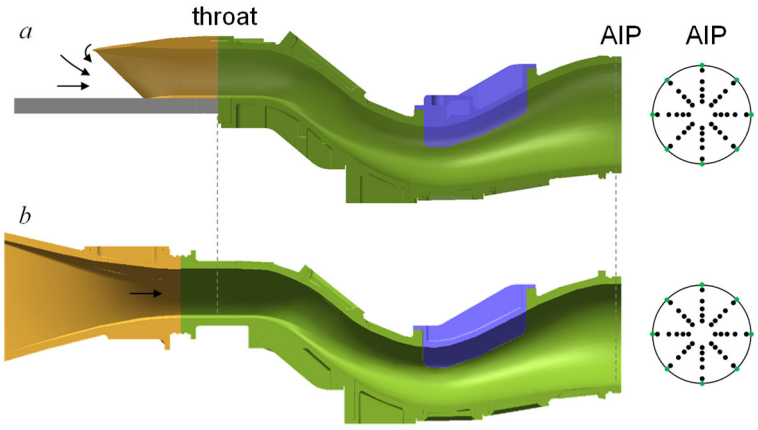

Figure 2. *Section view of the serpentine diffuser with a cowl inlet (a) and integrated in the wind tunnel [10] (b). AIP schematics on the right illustrates the 40-probe rake of dynamic pressure transducers (black) and 8 azimuthal static pressure ports (green).*

The total steady and dynamic pressures at the AIP are measured using a 40-probe array arranged in eight, equiangularly spaced rakes around the circumference of the AIP (Figure 2) according to the SAE industry standard ARP1420b (dynamic pressure rake provided by the Boeing Co.). Each probe comprises of a miniature high-frequency pressure transducer (*Kulite* XCEL-072), a differential transducer with a range of 170 kPa, and an accuracy range of +/- 850 Pa that enables simultaneous sampling frequencies up to 100 kHz. In the present experiments, the 40 transducers were sampled simultaneously at 25 kHz over a 10 second interval, providing a basis for the spectral analysis of the flow, while the total pressure tubes yielded the local time-averaged pressure. Each of the eight radial 5-probe rakes is matched with a corresponding azimuthal static pressure port on the inner surface of the diffuser (Figure 2). In addition, fifteen static pressure ports are distributed along each of the inner bottom and top surfaces of the diffuser wall. All the time-averaged static and total pressures are measured using a pressure scanner (PSI Netscanner) system using 100 sets of 64 independent samples across five scanner modules, each consisted of 16 pressure channels; hence each time-averaged pressure is based on the total of 6400 individual measurements. The estimated uncertainties of the mean pressures and of the derived $DPCP_{avg}$ parameter are less than 1% and 2%, respectively.

Stereo PIV measurements were employed to investigate the flow through the cowl inlet (Figure 3), where the orientation of the imaging plane is such that the bulk flow velocity component is the through-plane velocity component *u*. Three views of the PIV setup are shown in Figure 3, with the top view (Figure 3c) illustrating a section of the 19 mm thick, 1.91 m × 1.91 m ground plane (in blue), having an integrated 16 mm thick glass panel for PIV measurements inside the cowl inlet. A pair of Phantom VEO 710L cameras were used for the PIV imaging, along with the Photonics DM30 dual cavity high speed YLF laser, which can reach a frequency of 10 kHz and pulse energy of 65mJ. One of the biggest differences between this stereo setup and a 'typical' stereo setup is the angle of the cameras relative to the laser sheet. Typically, the camera is angled along one axis relative to the laser sheet, but the cameras in this setup are angled along two axes (Figure 3b and c). Because of this, the axis along which the Scheimpflug tilt must be applied is no longer obvious. It is still possible to fully correct for the angle and focus on the PIV plane, but the process is iterative. The tilt axis must be adjustable relative to the camera sensor, such that an optimal tilt angle can be found that corrects for both the angle of the lens shown in Figure 3b, and the angle shown in Figure 3c.

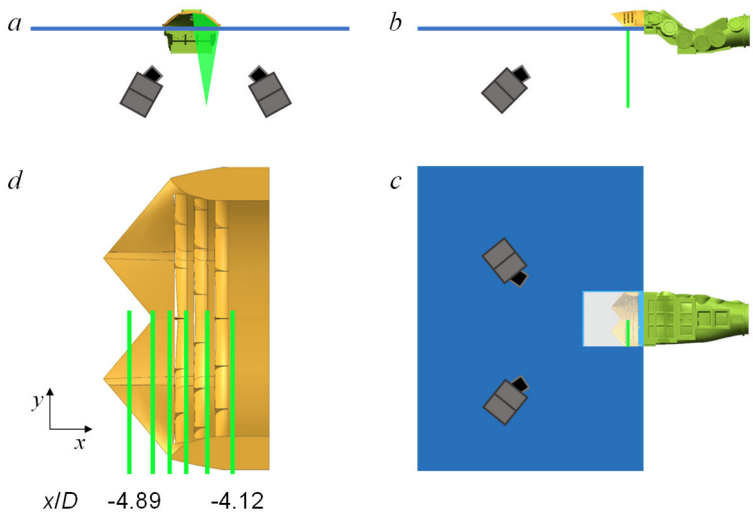

Figure 3. *Upstream (a), side (b), and bottom (c) views of stereo PIV cameras and laser sheet illumination, and spanwise projection of cross-stream and streamwise-normal sPIV planes (d) relative to the bleed slots on the surface of the cowl at x/D = -4.89, -4.7, -4.58, -4.43, -4.28, and -4.12.*

In the present experiments, the flow within the cowl and the diffuser is

controlled using arrays of spanwise slots on the surface of the cowl (Figure 3d), facilitating 'aerodynamic bleed' by exploiting an existing pressure difference on two sides of a body by adding a slot or a channel between them to enable flow from the high-pressure side to low-pressure side. This method has been implemented on airfoils [11] to reduce drag and/or increase lift, on and inlets to reduce losses associated with turning of air around an inlet with a sharp lip [Bore, 1993]. It has the inherent limitation that the flow rate cannot be controlled, as it is governed by the pressure difference and losses through the channel. However, they can be opened and closed dynamically, depending on flow conditions. It is known that in cowl inlets, flaps that open and close bleed slots (blow-in doors) are used to allow air through in subsonic flow, when the supersonic inlets have high losses (e.g., in the context of Harrier vertical and/or short take-off and landing (V/STOL) aircraft [4]. In the present work, three segmented bleed slots are integrated into the 'control' cowl model, otherwise identical to a nominal cowl geometry. The objective of such aerodynamic bleed is twofold. First, as indicated in 'auxiliary' inlet applications to cowl inlets [4], such openings increase the inlet area and introduce a secondary source of inlet flow, thereby weakening the cowl vortices formed off the cowl inlet geometry. However, as already addressed by Burrows et al. [9], the aerodynamic bleed slots in the present work are designed such to disrupt the cowl vortices right after their formation along the inner cowl surface and to sever their supply of vorticity off the surface by their premature deflection into the bulk diffuser flow. As seen in Figure 3d, the slots' passages have a bell-mouth-like contour to minimize losses, while being angled downstream on the inner surface. Figure 3d also illustrates six cross stream stereo PIV planes normal to the streamwise direction that cover just over a half the span of the cowl inlet, where the streamwise positioning of the three downstream measurement planes is aligned with the exit planes of the corresponding three bleed arrays. It is noted that the base/nominal cowl has the same geometry as the shown one with the bleed slots, only without any passages, and the PIV measurements are taken across the same six measurement planes.

III. The Base Flow

While the earlier work [10] considered the flow through a serpentine diffuser 'decoupled' from an inlet, effectively isolating the diffuser performance by minimizing the upstream flow nonuniformities, Burrows et al. [9] included a cowl inlet to the same diffuser geometry to mimic the full intake to an engine in static conditions (zero free-stream velocity) since it is known that such inlets are designed for other parts of the flight envelope and engender streamwise vortices during the takeoff that can significantly hinder the engine operation. As an illustration of the dramatic differences between the 'isolated' serpentine diffuser flow and its equivalent when the air is drawn through the cowl, Figure 4 shows the AIP contour plots of the mean total pressure at $M_{AIP} = 0.5$, as measured by the 40-probe rake. As already discussed in greater detail [10], in the absence of significant intake flow distortions, there is a localized flow separation along the upper surface, which trails into a pair of counter-rotating vortices that result in the localized total pressure deficit domain, as seen in the upper contour in Figure 4a. In addition, two lower-surface streamwise vortices, originating at the D-shaped diffuser inlet, interact and diffuse over the whole diffuser path, resulting in the weaker total pressure deficit along the bottom AIP face (Figure 4a). Overall, the total pressure loss, expressed as recovery $p_t/p_{t,o} = 0.961$, while axial nonuniformity results in a significant circumferential distortion parameter $DPCP_{avg} = 0.0345$. The effect of the cowl (Figure 4b) is rather dramatic on the mean flow field at the same AIP Mach number. Total pressure is reduced across the whole AIP face yielding the drop in recovery of over 14%. Interestingly and perhaps counter-intuitively, circumferentially averaged distortion descriptor of the mean flow field $DPCP_{avg} = 0.007$, as only a minor axial asymmetry is measured at the AIP (Figure 4b). These differences in the mean flow are attributed to the streamwise vortices engendered by the cowl. While the strong pressure losses are to be expected under such conditions, it is interesting that no significant topological features of vortices are present in Figure 4b, suggesting significant interactions, mixing, and unsteadiness that are associated with them at the AIP.

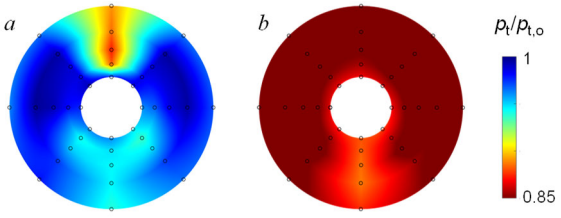

Figure 4. *Color raster plots of distributions of the total pressure at the AIP for the mean flow with the serpentine diffuser integrated in the wind tunnel (a) and with a cowl inlet (b) at $M_{AIP} = 0.5$.*

The integration of the diffuser with the serrated cowl inlet introduces inlet vortices that significantly alter the base flow as compared to that of the isolated diffuser with an inlet contraction. The serrated cowl inlet has four straight edges that form two triangular streamwise protrusions that connect at the center plane and at the corners of the cowl with the ground plane (Figure 5). These sharp edges engender two pairs of counter-rotating streamwise vortices- one pair about the center plane and a single vortex in each corner. The surface topology effected by these vortices is characterized using surface oil visualization at $M_{AIP} = 0.5$ and is

shown in Figure 5a and b, of the ground plane underneath the cowl and of the inner surface of the cowl (the flow is from top to bottom). The surface oil visualization on the ground plane (Figure 5a) shows a surface signature of the corner vortices, one of which is also marked by a yellow dashed line. This line is a near-surface interface of the corner vortices (*y*-direction streaks below line) with the bulk flow (*x*-direction streaks above line) and is moving away from the corner as it progresses in the streamwise direction, indicating that the corner vortex grows in size along its path. This visualization also shows the high angularity of the flow in the vortex indicated by the streaks in the corner that are perpendicular to the bulk, centerline flow (marked by *N*), creating an effective blockage in the flow because flow in this region is stagnant in the +*x* direction, resulting in reduced mass flow rate and total pressure recovery. The dark streaks that originate at the cowl's upstream edges are the surface signatures of the vortex cores (marked on one side by yellow dashed lines in Figure 5b) that proceed towards the center plane and each of the corners. It is apparent that the vortices are strong enough to produce near-wall flow that is orthogonal to bulk flow in the vortices, where some streaks near the corner and center plane have no streamwise component (near surface flow aligned with *y*- instead of *x*-direction, marked by *N*). This highlights the losses that the vortices engender – orthogonal streaks indicate an effective blockage in the flow, where there is zero velocity in the *x*-direction. In addition, secondary patterns are seen between yellow dashed lines and cowl edge, which are similar to those on a delta wing [12] and are attributed to secondary or tertiary separation and/or attachment lines. Overall, the cowl-induced secondary flows introduce a central counter-rotating vortex pair, and corner vortices merged with the same-sense outer cowl-induced vortices, as marked schematically at the downstream end of the cowl in Figure 5b.

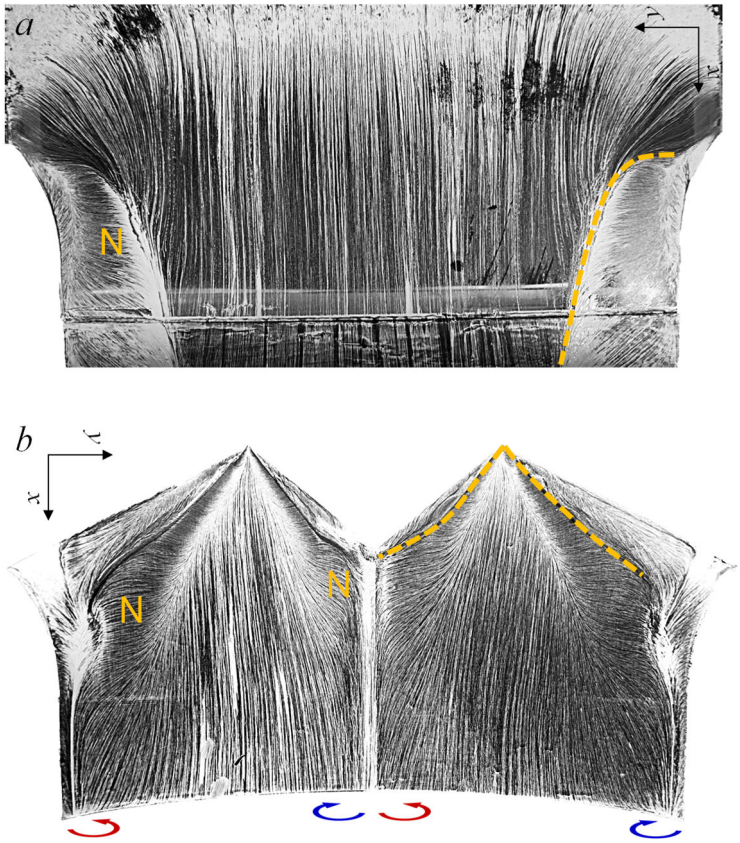

Figure 5. *Surface oil visualization on the ground plane (a) and the inner cowl surface (b) inlet to the serpentine diffuser at M_{AIP} = 0.5. Dashed lines highlight the initial vortex paths over one side of the inlet, while the flow domains indicating a local flow orientation normal to the streamwise direction are marked by the letter N on the opposite side of the inlet.*

The vortex formation and evolution of these dominant streamwise vortices was also characterized using stereo particle image velocimetry (sPIV) that was conducted at six cross stream planes normal to the streamwise direction (cf. Figure 3d). The axial locations of these measurement planes were selected relative to the bleed slots, as described in Section II, they are kept the same in the base flow in which the cowl geometry is the same by no slots are present. The PIV domain included just over half the span of the cowl inlet, for a check the flow symmetry. In the present experiments, the flow through each of these six planes is measured at M_{AIP} = 0.5 for the base cowl geometry since the maximum reachable AIP Mach number is 0.5 because of the high flow losses induced by the base cowl and the fixed blower power. Color raster plots of distributions of the streamwise vorticity ω_x and turbulent kinetic energy (TKE) q in the base flow within the sPIV measurement planes are shown in Figure 6a-f and Figure 6g-l, respectively, ordered from upstream (a,g) to downstream (f,l). Figure 6a shows the vortices originating on the edge of the serrated cowl. As these vortices extend in the streamwise direction, they are oblong in shape and follow the cowl edge until the edges either connect at the centerline (Figure 6b) or connect to the corner (Figure 6c). When the cowl edges connect at the centerline, the individual vortices of opposite sense coalesce into a counter-rotating vortex pair that remains at the centerline (Figure 6d-f), where the centerline vortex fully in the sPIV domain is rotating counterclockwise. The corner vortex rotates clockwise and remains in the corner through all planes. In the final two planes (Figure 6e,f), lower vorticity levels are apparent, which coincide with higher TKE levels (Figure 6k,l), indicating that the vortices are exhibiting

increasing turbulent fluctuations, arguably associated with mixing. The TKE in Figure 6g-l shows the turbulent fluctuations associated with each pair of vortices. The center plane vortices have more fluctuation energy than the corner, but both regions have significantly more turbulent energy than the bulk flow in the rest of the field, in which the magnitude of the TKE is negligible. Turbulent fluctuations are most concentrated in the more upstream planes (Figure 6h-j), where there are small regions of high energy (central vortices), after which those regions grow with the vortices into larger regions with lower TKE as the flow progresses through the cowl.

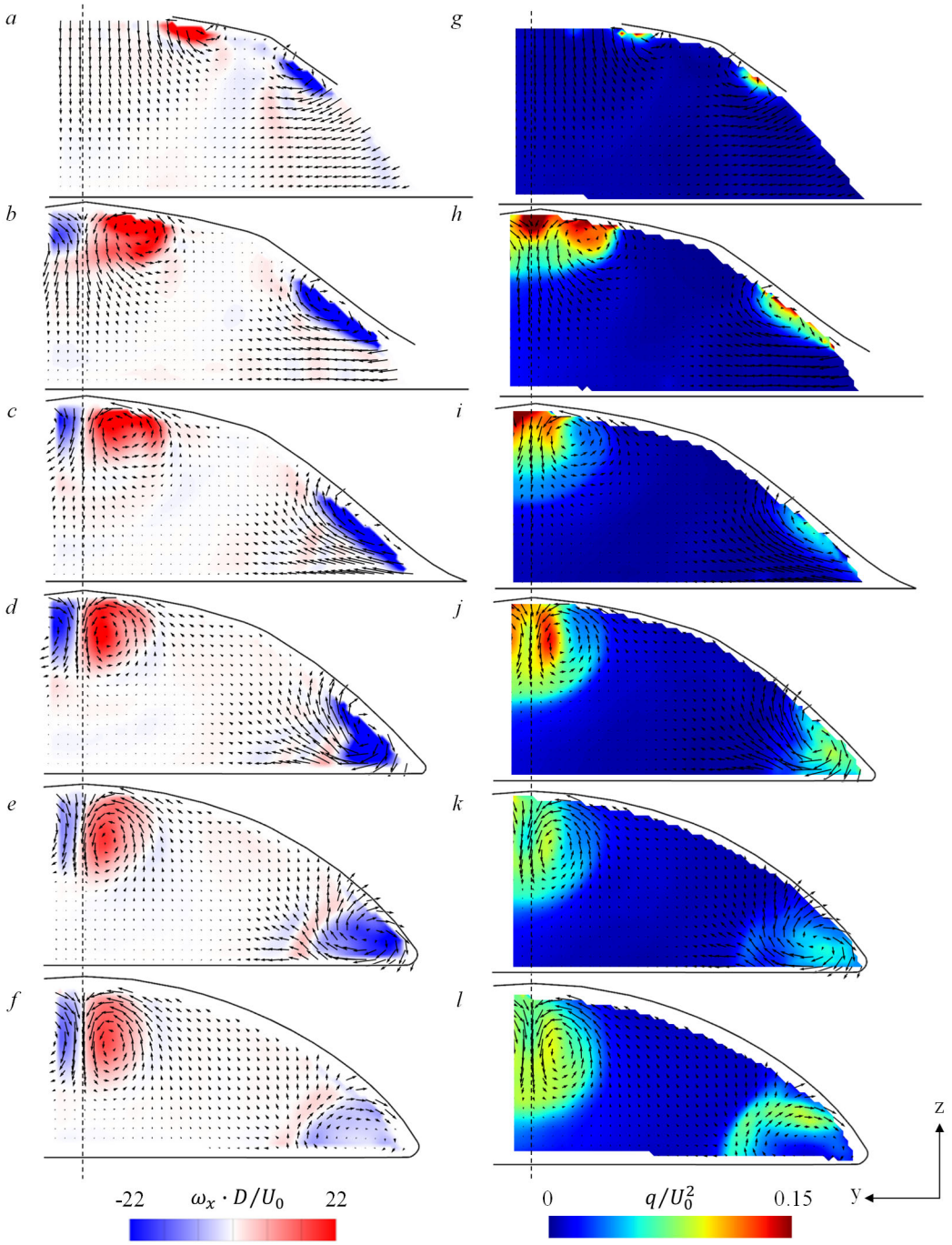

Figure 6. *Color raster plots of distributions of the streamwise vorticity (a-f), and TKE (g-l) of the base flow within the spanwise planes at x/D = -4.89 (a, g), -4.7 (b, h), -4.58 (c, i), -4.43 (d, j), -4.28 (e, k), -4.12 (f, l), at M_{AIP} = 0.5. The dashed line in each image marks the centerline y = 0, and solid lines bounding the domains mark the intersection of the diffuser's inner surface with the measurement planes.*

While the earlier work [9] also utilized time-resolved measurements of the rake's total pressures, an important finding is emphasized here with respect of the estimates of the total pressure distortion and recovery based on the mean total pressures of the time-resolved measurements and the steady total pressure measurements of the highly unsteady diffuser flows, such is the base flow with the cowl inlet. First, the unsteady characteristics of the flow at the AIP are revealed by using time-resolved measurements of the total pressure over a range of M_{AIP} using a dynamic pressure rake described in Section II. The time-resolved total pressure is used to compute the instantaneous and time-averaged circumferential total pressure descriptor $DPCP_{avg}$ and pressure recovery. The disparities between the time-average and instantaneous distortion and pressure recovery are compared in Figure 7. Each parameter is calculated in two ways: based on the time-averaged total pressure (in this discussion this is coined steady-state) and is also calculated on the series of instantaneous total-pressure realizations and then averaged (time-averaged, in this discussion). To further clarify the difference, steady-state is calculated as $X(\bar{p})$, and time-average is calculated as $\overline{X(p)}$, where X is a calculated parameter, p is the instantaneous pressure, and the bar notates a time-average. In addition to these calculations, the 95% confidence interval representing 95% of the range of instantaneous parameter values is shown by the shaded region in the plot. The confidence interval is calculated with percentiles to produce range of parameter values from the 2.5% to 97.5% percentiles. Such parameters and their confidence intervals in the range $0.12 \leq M_{AIP} \leq 0.5$ are shown in Figure 7.

The data in Figure 7a show that there is a significant disparity between the steady-state $DPCP_{avg}$ and its corresponding time-averaged and 97.5% percentile values. The steady-state $DPCP_{avg}$ is very low throughout the range of M_{AIP} (less than 0.007 at $M_{AIP} = 0.5$) as anticipated from the relative uniformity and axial symmetry of the total pressure distributions at the AIP, as already seen in Figure 4b. However, the time-averaged distortion is significantly higher, reaching about 0.025 at $M_{AIP} = 0.5$. Besides the disparity in magnitudes, there is also a difference in the rate of change of the distortion with M_{AIP}, where the top bound of the confidence interval (97.5% percentile) increases at a much steeper rate than the steady state $DPCP_{avg}$. The distortion unsteadiness also increases with M_{AIP} as is evidenced by the increasing width of the confidence interval (e.g., from 0.002 at $M_{AIP} = 0.12$ to 0.02 at $M_{AIP} = 0.5$). Similar to the variation of the total pressure distortion with M_{AIP} in Figure 7a, the variation of the pressure recovery PR is shown in Figure 7b. These data show that PR decreases nearly linear with M_{AIP}, exceeding a 10% loss already at about $M_{AIP} = 0.375$. In this case, the time-average PR coincides with the steady-state PR because the parameter is linear, meaning the two methods of calculation discussed above result in the same value, unlike $DPCP_{avg}$. Also, like with distortion, the instantaneous variation in pressure recovery increases with M_{AIP}.

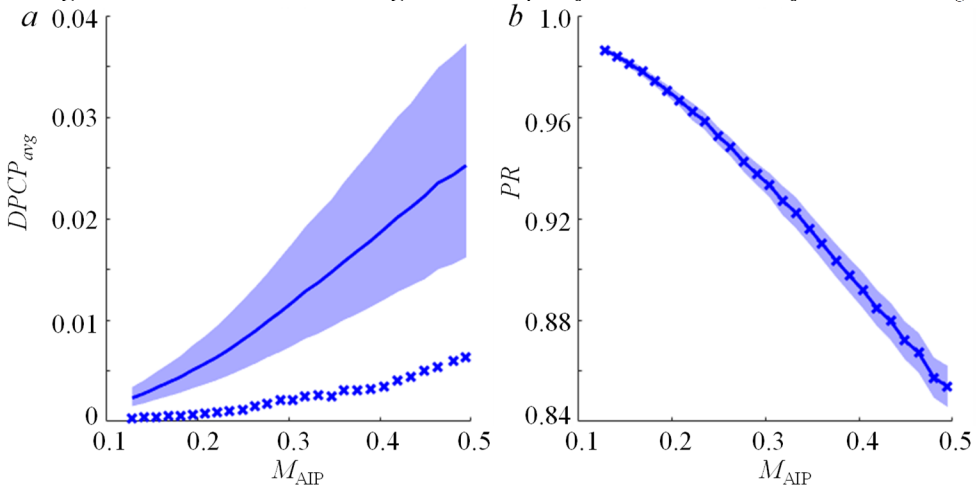

Figure 7. *Steady state (×) and time-averaged (—) circumferential distortion $DPCP_{avg}$ (a), and pressure recovery PR (b), for $0.12 \leq M_{AIP} \leq 0.5$. The 95% confidence interval is marked with a blue shaded region about the time-averaged data.*

Figure 4b indicated that there is a significant loss of total pressure at the AIP, and that the time-averagted loss is nearly uniformly distributed across the AIP face, except at its lower central region that exhibits a slightly lower drop in pressure. As discussed in connection with Figure 7, there are significant instantaneous deviations from the time-averaged total pressure distributions. Distributions of the instantaneous total pressure at an instance in time that correspond to the maximum $DPCP_{avg}$ are plotted in (Figure 8a-c) for $M_{AIP} = 0.3$, 0.4, 0.5 and are highly nonuniform and asymmetric. However, when considering the 40-probe average of the total pressure, the instantaneous measurements do not differ much from the time-average values, which is corroborated by the small variation of pressure recovery

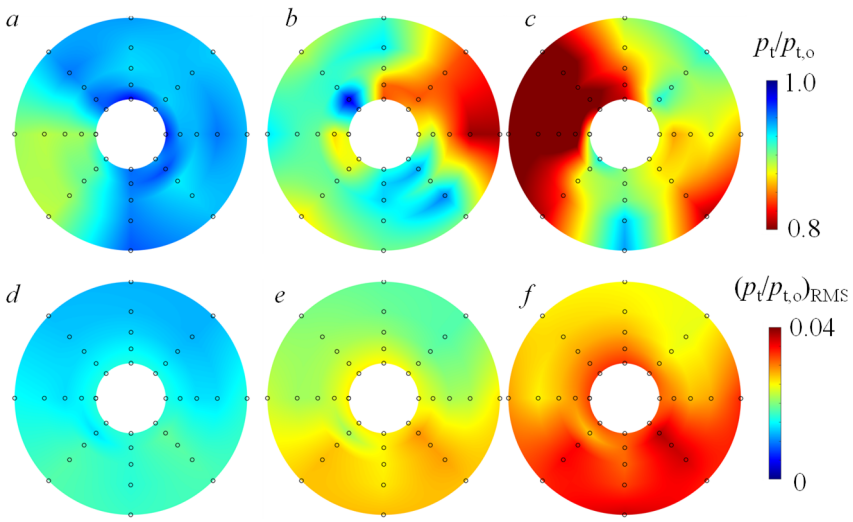

Figure 8. *Color raster plots of the total pressure distributions at the AIP at the instant of peak $DPCP_{avg}$ (a, b, c) and AIP total pressure RMS fluctuations (d, e, f) for M_{AIP} = 0.3 (a, d), 0.4 (b, e), 0.5 (c, f).*

shown by the confidence interval in Figure 7b. This highly non-uniform distribution results in high instantaneous circumferential distortion that clearly becomes worse with increasing M_{AIP} (cf. Figure 7). The unsteadiness of the AIP total pressure is evident in color-raster plots of the RMS of the total pressure fluctuations shown in Figure 8d-f. It is noteworthy that the RMS fluctuations are consistently higher along the lower segment of the AIP over the full range of M_{AIP}. It is seen in the streamwise evolution of the four dominant vortices in Figure 6 that the vortex pair becomes advected and convected away from the top surface, while the corner vortices keep evolving along the bottom corner sides. Even further downstream, as previously shown in numerical simulations [9], each vortex of the vortex pair destructively interacts with the closest corner vortex and hence to dominant vortical interaction remains confined to the bottom lower portion at the AIP, as also evidenced in the total pressure RMS measurements in Figure 8.

Further analysis of the total pressure unsteadiness at the AIP is expressed through spectral magnitudes (up to 10 kHz) of the total pressure fluctuations measured at M_{AIP} = 0.5 by each of the AIP dynamic sensors, as shown in Figure 9b. The data are arranged in vertical bars and the sensors are grouped in each of the circumferential rings of the array as shown schematically in Figure 9a (the data for each sensor are arranged in CW order starting at the red line in Figure 9a and the bar for the first port is repeated at right the end of the group). These data show that the power levels are fairly uniform in value for frequencies up to about 2 kHz, where the power drops by an order of magnitude. When comparing the variation in the angular direction, the outer two rings (rings 4 and 5) show that the portion at the top half of the AIP (left half of each ring group in plot) has a lower power than at the bottom half of AIP, which is consistent with the corresponding RMS AIP distributions in Figure 8f. This trend can also be identified in ring 3, but to a lesser extent. At the innermost rings, there is high azimuthal uniformity, indicating that there are not particular spatial differences in the fluctuations in the inner core flow. For comparison, analogous spectral representation is shown in Figure 9c for the flow through the same diffuser geometry at the same M_{AIP} = 0.5, only in the absence of the cowl inlet, where the diffuser is integrated into the wind tunnel flow, as already discussed in connection with Figure

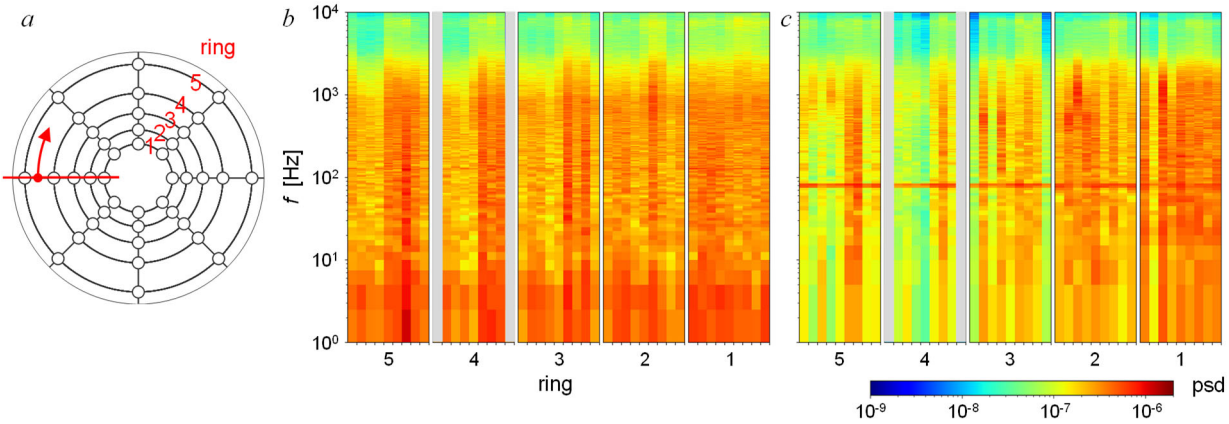

Figure 9. *Vertical color raster bars of spectral magnitudes of the total pressure for the diffuser with a cowl inlet (b) and integrated into the wind tunnel (c) measured by AIP transducers at $M_{AIP} \approx 0.5$ along each of the circumferential rings and arranged in CW order as marked in (a). The bars shaded in gray represent missing data.*

4. Besides the noise (non-flow) spectral peak across all the sensors at about 90 Hz, the major difference is seen across the two outer rings, closest to the surface, where significant suppression of the pressure fluctuations is seen around the circumference, except, at a lesser degree at the bottom of the AIP domain. The weak signature of the mean total pressure deficit in that region (Figure 4a) indicates that the flow structures/vortices at the bottom of the AIP are both weak and weakly unstable. It is interesting that the more impactful deficit associated with the localized flow separation in the upper central AIP domain (Figure 4a) appears to be fairly stable close to the surface, as indicated in the spectra across the Rings 5 and 4 in Figure 9c. However, crossing towards the bulk flow away from the surface, unsteadiness of the pressure fluctuations increases towards Rake 1 (Figure 9c), clearly indicating that the most energy in fluctuations is the inner flow. Considering the mean total pressure deficit (Figure 4a), it can be postulated that the increased unsteadiness may be result of the interactions between the upper and lower flow structures/vortices which sufficiently grew by the AIP off the upper and lower diffuser surfaces.

IV. Dynamics of the Controlled Flow

Guided by the sharp drop in the total pressure along the inlet section of the cowl [9] and an indication that the counter-rotating vortex pair along the upper surface (cf. Figure 6) creates a stagnation zone upon entering the diffuser, it is decided that the flow control should focus on disruption of this vortex pair formation along the cowl upper surface. To facilitate this, three autonomous bleed slots are opened across the cowl upper surface, as schematically shown in Figure 10a. They utilize the existing pressure difference across the outer air and the inner flow drawn into the diffuser. In principle, these slots can be equipped by louvers and commanded to open and close, but in the present experiments they are kept open at all times for the current proof-of-concept study. The entrance to the slots on the outer side is bell-mouth-like to minimize pressure losses, and on the flow-side they are contoured to guide the airflow smoothly into the cowl, right at the vortex pair formation region, aimed at the vortex disruption, in an effort to bypass the sharp loss in the total pressure in that region.

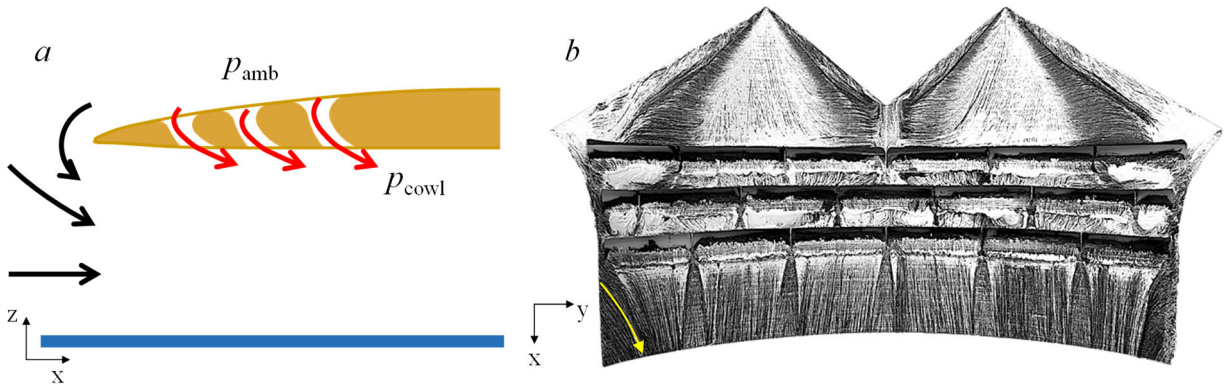

Figure 10. *Schematics of intake flow through the cowl inlet with the three bleed slots (a), and oil-flow visualization on the inner surface of the cowl at $M_{AIP} = 0.5$. Yellow arrow highlights direction of oil streaks in the corner downstream of slots.*

The effect of the bleed through the cowl slots is first investigated using surface oil visualization, and the topology of the oil streaks on the curved inlet surfaces at $M_{AIP} = 0.5$ is shown in Figure 10b (equivalent to the base flow visualization in Figure 5b). Though the topology upstream of the slots is similar to that of the base flow, there are some differences. In particular, the upstream slot appears to create blockage as is evidenced by the fact that the oil streaks are parallel to the slots along the upstream edge of the first slot, which is most noticeable near the center plane. Another observation is that the darker streaks that mark the vortex position along the two outer cowl edges are closer to the edge of the cowl lip than in the base flow. It is conjectured that this is the case because the slots effectively provide a flow bypass to the cowl inlet so that the flow rate through the front inlet face is lower. In addition, though somewhat obfuscated by the slots, it appears that the flow downstream of the slots is straighter than in the base flow. It should be noted that some flow angularity is present in the wake of the structural fins that partition the slots for support. The biggest difference between oil-flow visualization of the base flow (Figure 5b) and the slotted cowl inlet (Figure 10b) downstream of the slots is the direction of the flow in the corners. In the presence of the bleed flow through the inlet, the streaks are directed towards the centerline (as marked by the yellow arrow), rather than towards the corner as in the base cowl in Figure 5b. This change associated with the trajectory of the corner vortex is further characterized using stereo PIV measurements.

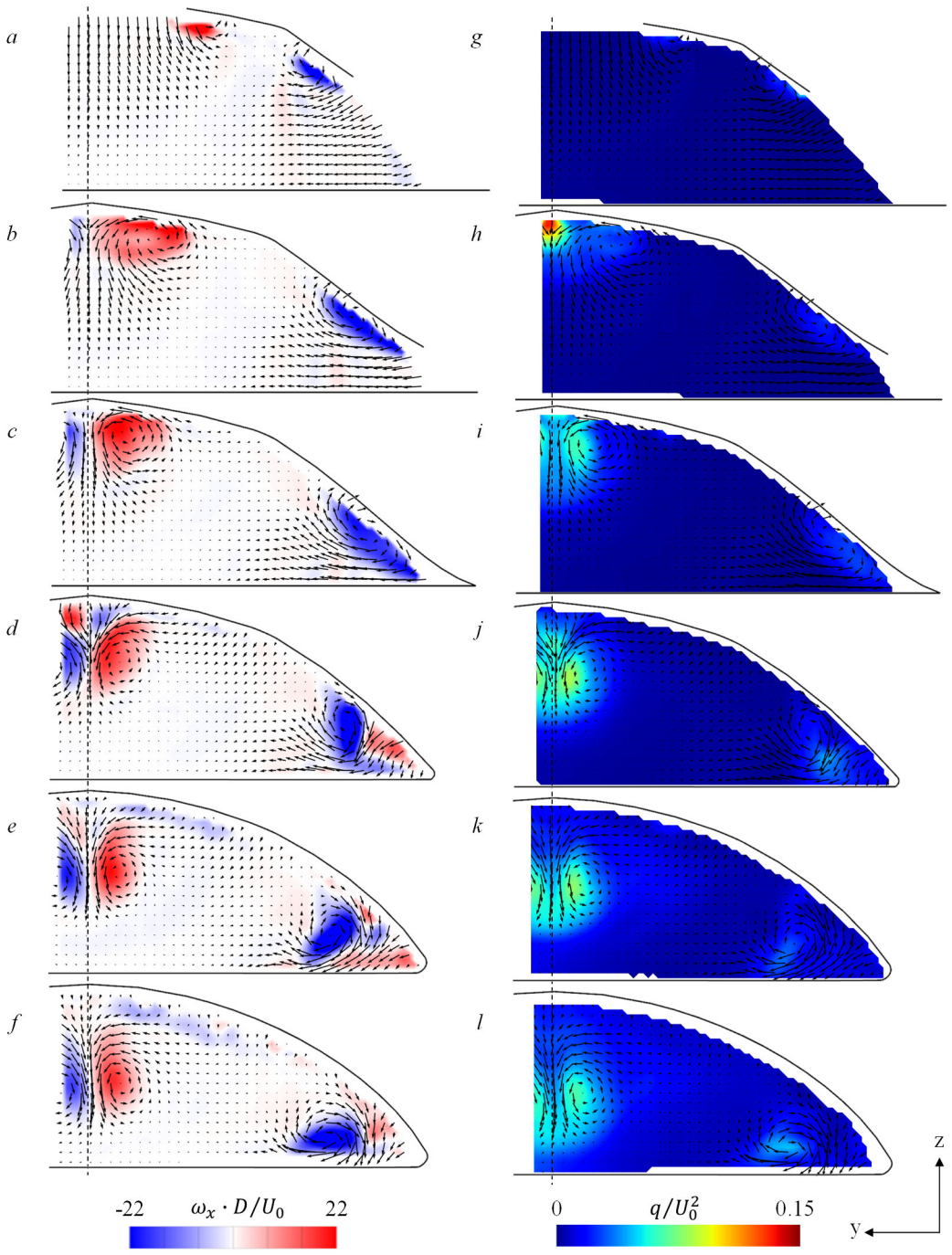

Figure 11. *Color raster plots of vorticity (a-f), and TKE (g-l) fields within the slotted inlet cowl, within the spanwise planes at x/D = -4.89 (a, g), -4.7 (b, h), -4.58 (c, i), -4.43 (d, j), -4.28 (e, k), -4.12 (f, l), at M_{AIP} = 0.5. Dashed line is the test section centerline y = 0, and the bounding solid lines mark the intersection of the diffuser's inner surface with the measurement planes.*

The effects of the cowl bleed slots are investigated using sPIV at the same planes as in the base flow in Figure 6. The bleed flow through the slotted inlet has significant effects on the evolution of the strength and scale of the streamwise vortices that form in the base cowl flow as shown in Figure 11a-f. While the vorticity distributions in the measurement planes upstream of the slots in Figure 6a-c and Figure 11a-c are similar, their evolution downstream of the slots is notably different. The additional momentum flux and concomitant vorticity effected by the flow through the slots along the upper cowl surface alters the trajectory of the center vortex pair by displacing them farther away from the top surface compared to the base flow. The additional momentum flux near the surface corners of the cowl

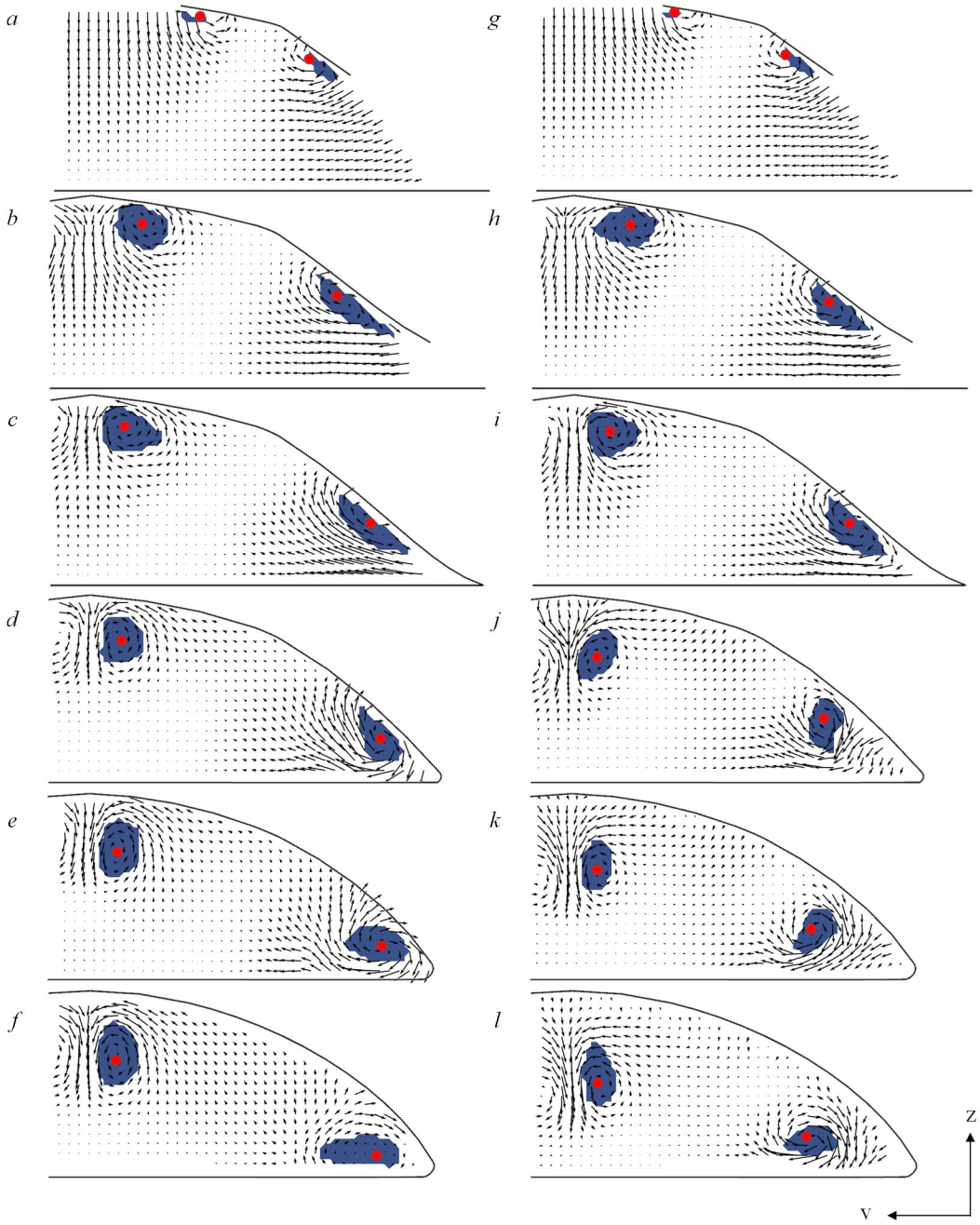

Figure 12. *The extent of the vortex cores (blue shading) and the vortex centers (red dots) in the flows through the base cowl (a-f, cf. Figure 6) and the cowl with the autonomous bleed (g-l, cf. Figure 6.14), at x/D = -4.89 (a, g), -4.7 (b, h), -4.58 (c, i), -4.43 (d, j), -4.28 (e, k), -4.12 (f, l).*

alters the vorticity distributions within the cores of these vortices, which rotate through the measurement planes as they are advected away from the corner towards the bulk flow, as seen in Figure 11d-f. Furthermore, the bleed flow effects also lead to a clear reduction in the turbulence intensity within and around the cores of the streamwise vortices as shown by the distributions of TKE in upstream and downstream of the slots, in Figure 11g-l. Similar to the base flow, TKE spreads about the cores and dissipates as the flow progresses downstream.

The effect of the bleed on the position and extent of the cowl lip vortices is quantified using vortex scalar functions Γ_1 and Γ_2, respectively [13-15], where the extent is defined as the boundary or domain of the vortex. The Γ_1 and Γ_2 dimensionless scalars are computed using $\Gamma_1(\boldsymbol{x}) = \frac{1}{S}\int_{\boldsymbol{x}'\in S} \sin\alpha \, d\boldsymbol{x}'$ and $\Gamma_2(\boldsymbol{x}) = \frac{1}{S}\int_{\boldsymbol{x}'\in S} \sin\beta \, d\boldsymbol{x}'$, respectively, where S is a circle with center x and a chosen radius R, which is an adjustable parameter. For every point within that circle

of radius R centered at point x, the sine of an angle is integrated and then divided by the area of S. The angle used in Γ_1, α, is defined as the angle between the vector pointing from x to x' and the velocity vector at x', $u(x')$. In the angle β, the absolute velocity vector $u(x')$ is replaced with a velocity relative to that at x, or $u(x') - u(x)$. As defined, both scalars vary from -1 to 1, and the peak value of both criteria is reached at the vortex center. The Γ_1 and Γ_2 criteria are computed for every point in the PIV-measured flow field, such that regions without vortices have low Γ_1 and Γ_2 magnitudes, while regions within vortices have higher values. To identify the extent of each vortex, the criteria are thresholded by $|\Gamma_1| > 0.75$ and $|\Gamma_2| > 0.75$. When these criteria are satisfied at a given point in the measurement plane, this point is considered a part of the vortex domain. While the choice of this threshold affects the defined absolute vortex domain size, the trends used for analysis remain the same. The center of the vortex is found by finding the Γ_1-weighted centroid of the previously defined extent, where a weighted centroid is defined in $x_{wc} = \sum_{i=1}^{N} x_i P_i / \sum_{i=1}^{N} P_i$ for N points that each have a location x_i and a property P_i. This method was chosen to reduce possible noise associated with instantaneous PIV measurements. The computed centers and extents of the vortices shown in Figure 6 and Figure 11 are shown in Figure 12a-f and g-l, respectively. In connection with the discussion of Figure 6 and Figure 11, Figure 12 shows that the slots effect a change in trajectory of both the center vortices and the corner vortex. In addition, the vortex extents in the case with the slotted inlet (Figure 12g-l) are smaller for both the center and corner vortices, in particular starting in the fourth plane x/D = -4.43 (Figure 12d,j), which is just downstream of the first inlet slot (cf. Figure 3d). The smaller vortex cores in the presence of the bleed flow effects overall lower losses, as a larger ratio of the inlet flow is not in the vortex cores and has a higher streamwise (x-direction) momentum. The difference is most noticeable in the most downstream plane, after all three slots, in Figure 12f and l.

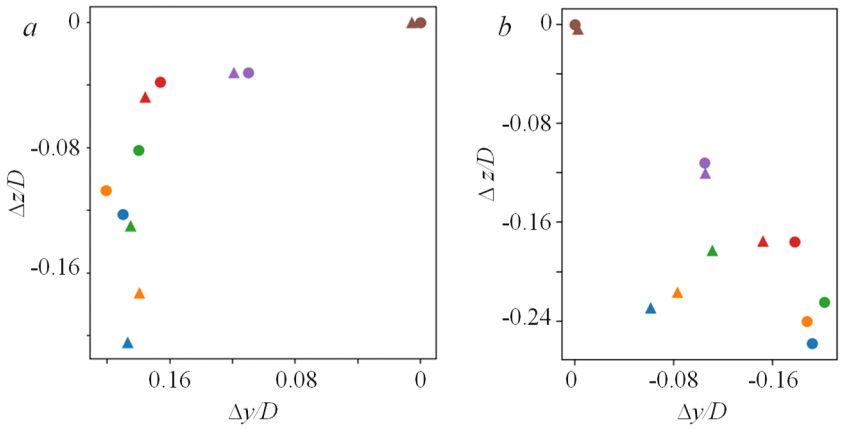

Figure 13. *The change in the y and z positions of the centers of the vortex cores relative to the vortex position in the base flow plane at x/D = -4.8 (●), and scaled by D, for center vortex pair (a) and the corner vortices (b) for base (●) and the controlled inlet (▲) at x/D = -4.89, -4.7, -4.58, -4.43, -4.28, -4.12.*

The trajectories of the vortex centers computed using the Γ_1 criterion (cf. red dots in Figure 12) are shown in Figure 13, with their position being relative to the base flow vortex position in the plane x/D = -4.8 [notice the position of this reference vortex is at (0,0)], and this relative position being scaled by the AIP diameter D. These data highlight first how the positions of the center (Figure 13a) and corner (Figure 13b) vortices are similar between the base and slotted cowl for the first three planes (x/D = -4.89, -4.7, -4.58), which are all upstream of the bleed slots. As can be seen in Figure 12, the center vortex is engendered on the serrated cowl lip and follows the lip towards the centerline as the edges of the serrated inlet converge at the center plane of the cowl (cf. Figure 5b). The base and controlled vortices are essentially in the same position through plane x/D = -4.58 (Figure 12d and j) where it becomes apparent that in the presence of the bleed, the vortex is moving away from the wall at a greater rate than that of the base flow. The disparity is the greatest in the plane x/D = -4.12 (Figure 12f and l), where there the vortices in the base cowl flow and in the presence of the bleed are offset by about 0.1D. While the effect of the bleed flow on the center vortex pair is primarily in the increased z-direction displacement relative to corresponding vortices in the base flow, there is a significant change in the position of the corner vortex past the measurement plane x/D = -4.58. While the corner vortex in the base flow resides within the corner (bottom right) along the cowl as is evidenced by the corner vortex position in the last three planes indicated in Figure 13b, in the presence of the bleed, the vortex deviates from the base flow trajectory by taking a turn at x/D = -4.43. At the most downstream PIV plane x/D = -4.12**,** it becomes displaced by greater than 0.1D in the y direction relative to the center of the corner vortex in the base flow.

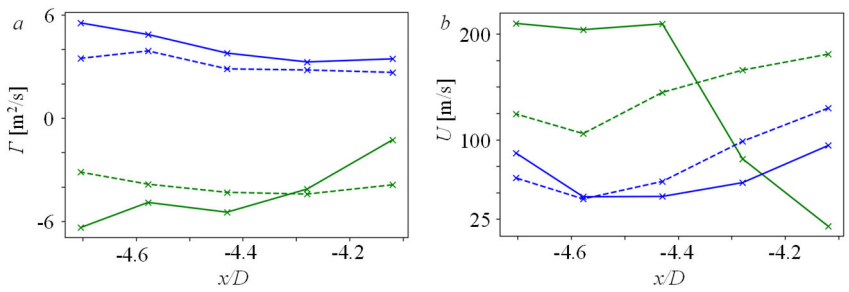

Figure 14. *The circulation Γ of the streamwise vortices (a) and the corresponding streamwise velocity U through their cores as defined in Figure 12 (b) for the center and corner vortices in the base cowl (solid lines) and the cowl with the bleed control (dashed lines).*

The streamwise variation of the circulation Γ, a measure of the vortex strength, is calculated as $\Gamma = \iint_S \omega \, d\boldsymbol{S}$ about the vortex cores in Figure 12 in the absence and presence of the bleed through their cross sections (Figure 14a). In addition, the streamwise component (x-direction) of velocity through the vortex cores in Figure 12 is computed and shown in Figure 14b. The streamwise variation of the circulation Γ of the corner and center vortices ($\Gamma > 0$, is counterclockwise) is shown in Figure 14a. These data show that the circulation of the streamwise center vortices diminishes nearly monotonically and that in the presence of bleed leads to a reduction in Γ arguably due to the reduction in the flow rate through the inlet. The respective circulations of the corner and center vortices in the absence and presence of bleed are similar in magnitude except that at $x/D > -4.3$ the circulation magnitude of the corner vortex in the absence of bleed decreases below the level of the circulation in the presence of bleed. This could be due to unsteadiness in the vortex in the base flow, as compared to a steadier vortex in the corner of the actuated flow where the vorticity remains more concentrated on the average. The variation of streamwise velocity U through the vortex cores in Figure 14b shows that while the trend of U in the center vortices is nearly unchanged in the presence of bleed (a reduction through $x/D = -4.58$ is followed by monotonic increase), there is a significant reduction in U in the corner vortex. However, for $x/D \approx -4.43$, U of the base flow decreases abruptly where the vortex that forms on the other edge of the serrated cowl inlet merges with the corner vortex as shown in Figure 5b. In fact, U in this vortex continues to drop through $x/D = -4.12$. In contrast, in the presence of bleed, U of the corner vortex is initially lower than base flow, partially because of flow bypass through the bleed ports, but U increases monotonically and at a similar rate as the increase in the center vortex.

Instantaneous PIV measurements are utilized to investigate the time variation in the position of the vortex centers, for the base and the slotted inlet cowl (Figure 12b-f and g-l). The Γ_2 and Γ_1 criteria discussed in connection with Figure 12 are used to determine the distributions of the vortex centers using each instantaneous velocity field out of 6,000 realizations. These distributions are used to form a 2D probability density function (pdf), where the integral of the two-dimensional distribution equals 1, like a conventional one-dimensional pdf. A method called Highest Density Region (HDR), outlined by Hyndman [16], is used to draw a boundary which describes the region of 75% of the realized positions. These regions which statistically represent 75% of the realized vortex positions are plotted in Figure 15 for planes x/D = -4.7, -4.58, -4.43, -4.28, and -4.12 in the absence and presence of bleed, in addition to the statistical mode (the most probable point), marked by solid circles. In the planes before the first bleed slot (x/D = -4.7, -4.58), the distributions of vortex positions in the base (Figure 15a) and controlled (Figure 15b) are quite similar. As they progress downstream, they begin to diverge, which highlights the effect of the slots on the inlet cowl vortices. The corner vortex moves away from the corner, and the central vortex is displaced further away from the top wall where it was engendered. In addition to these effects which

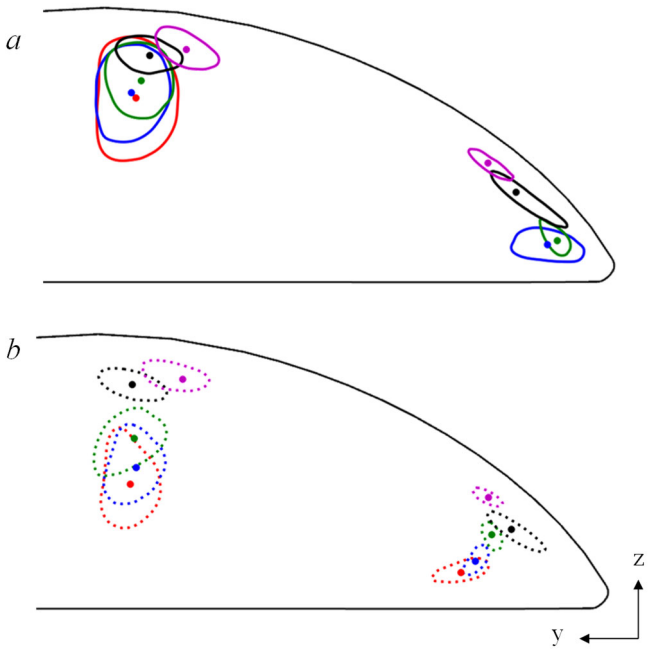

Figure 15. *Highest density regions [16] representing 75% of the distribution of the vortex positions in the base (a) and the inlet cowl with bleed (b) at x/D = -4.7, -4.58, -4.43, -4.28, -4.12, where the most probable point (mode) is marked with a solid circle.*

can be also observed with time-averaged sPIV data, Figure 15 shows the relative shape and size of the instantaneous distributions of vortex positions as they evolve through the planes. In the corner, the base flow distribution of vortex locations produces an oblong shape, which aligns with the cowl lip to which the vortex is fixed in the first two upstream planes (x/D = -4.7, -4.58). As it progresses downstream, at first the distribution tightens, indicating less unsteadiness, but later increases again (blue contour in corner of Figure 15a). The vortex distributions associated with the slotted inlet however maintain a small-sized distribution, indicating not only lower absolute unsteadiness through all PIV planes, but also a streamwise increase as was seen in the base flow. This effect is also observed with the central vortex. At first, the vortex position is fairly steady when it is locked to the cowl lip, but when it starts to separate from the wall, the base flow vortex position varies widely, with unsteadiness further increasing with each PIV plane, as indicated by the size of the areas enclosed by the HDR contour lines. The central vortices are rendered much steadier under the bleed control, which is indicated by the smaller-area regions (dashed contours) and has the greatest difference to the base flow in the two most downstream planes (shown in blue and red contours).

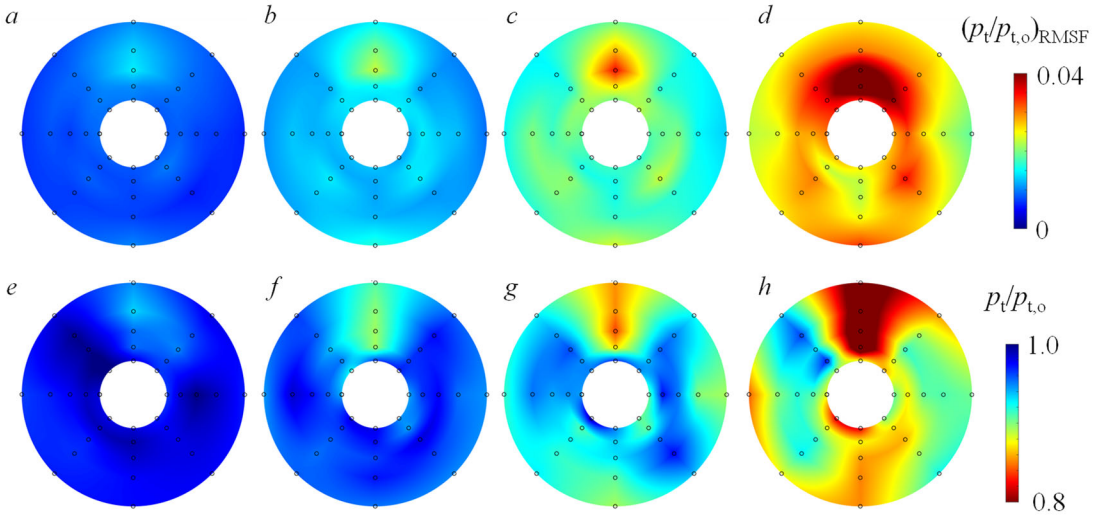

Figure 16. *Color raster plots of the RMS fluctuations of the total pressure (a-d) and total pressure distributions associated with peak DPCPavg distortion (e-h), at M_{AIP} = 0.3 (a,e), 0.4 (b,f), 0.5 (c,g), 0.6 (d,h) in the presence of bleed control.*

In addition to time-average measures, characteristics of the time-resolved total pressure at the AIP yield AIP distributions of the RMS total pressure fluctuations (Figure 16a-d) and of the instantaneous total-pressure associated with maximum $DPCP_{avg}$ (Figure 16e-h) for M_{AIP} = 0.3, 0.4, 0.5, and 0.6. Comparison of the RMS fluctuations of the total pressure at the AIP in the presence (Figure 16a-c) and absence (Figure 8a-c) of bleed, noting that M_{AIP} could not be attained for the base flow due to the losses, shows two main differences. First, the magnitude of the RMS fluctuations is much lower than in the base flow for all M_{AIP}, indicating lower unsteadiness of the streamwise vortices in the flow. This enhanced stability of the vortex cores may be related to the lower TKE in their cores as they are formed at the inlet (Figure 11). Secondly, the topology of the distribution of the total pressure is different in the presence of bleed. These data show a distinct peak of RMS fluctuations in the top center of the AIP, which is reminiscent of the distribution of the base of the isolated diffuser in the absence of the cowl [10]. This peak could be associated with the formation of a pair of counter-rotating streamwise vortices, which form along the separation at the second turn, which is also evidenced by the time-averaged total pressure topology at the central upper AIP domain in Figure 4a.

The differences between the spectral content of the total pressure fluctuations at the AIP are compared in the absence and presence of the bleed using color raster bar plots of power spectral density as shown in Figure 17 (similar to Figure 9 for the base flow). These data show that in the presence of bleed there is a spectral peak at about 90 Hz in the spectra of all the AIP sensors which is attributed to noise from the tunnel blower. It is noted that this spectral component is not detected in the absence of bleed (Figure 9a) because it is masked by the higher energy of the pressure fluctuations. In agreement with the discussion in connection with Figure 16, the spectral data in Figure 17 show that the power in the fluctuations is reduced significantly over the entire AIP plane and at almost all frequencies. Certain ports stand out as having an elevated fluctuation level, the highest of which is port number (3,3), which is marked with a rectangle in Figure 17a,b. Figure 17 also includes color raster plots of the AIP total pressure distributions in the absence and presence of bleed in Figure 17c and e, AIP total pressure RMS fluctuations shown in Figure 17d and

f, and corresponding spectra for the single sensor (3,3) are shown in Figure 17g. The spectra at port (3,3) shows that in the presence of bleed, the spectral power of the pressure fluctuations between 100 Hz and 1000 Hz actually increases, with a spectral peak occurring at about 250 Hz. It is conjectured that the increased fluctuations result from interaction between a pair of adjacent vortices near the upper surface that would normally be smeared out in the base flow. Other regions of elevated pressure fluctuations are noticeable in rings 1 and 2 (cf. Figure 17b), at the upper half of the AIP, which correspond to sensors (1-2, 1), (1-2. 2), and (1-2, 8) shown in the left half of the bar plot in each of the ring groups in Figure 17b.

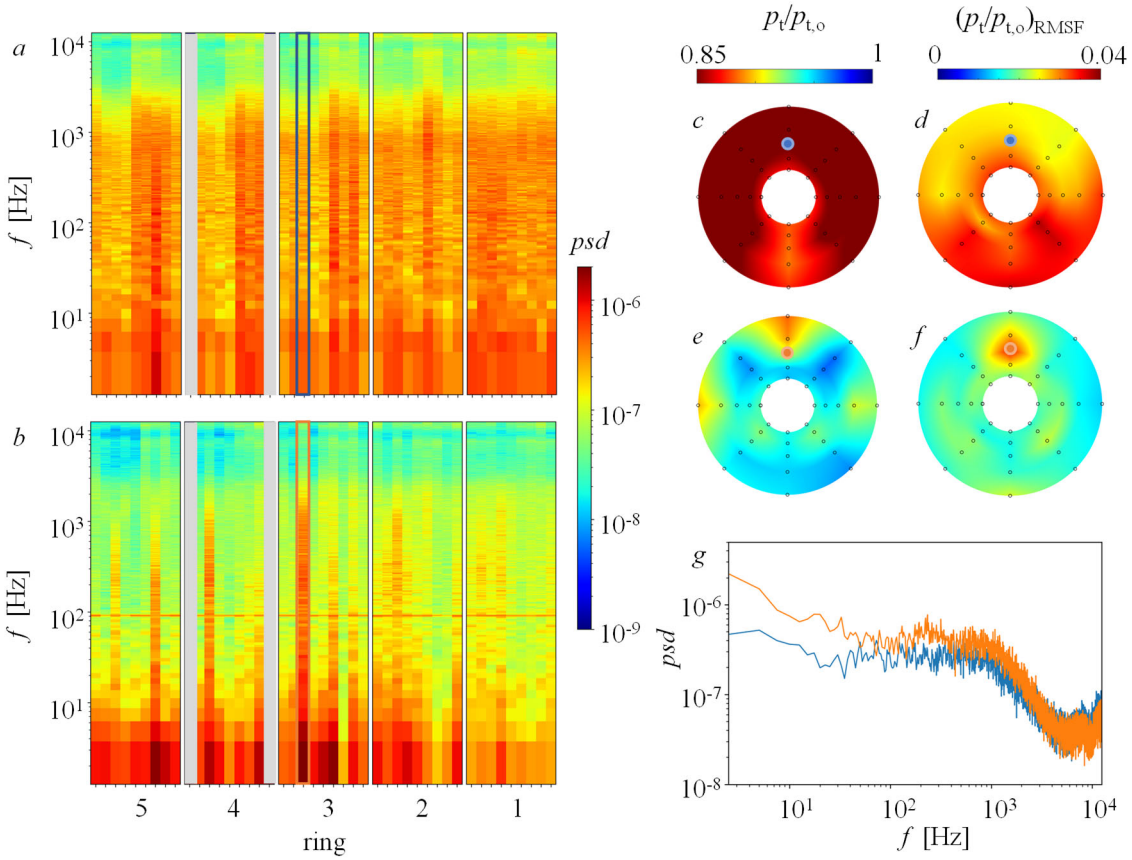

Figure 17. *Vertical color raster bars of spectral magnitudes (up to 10 kHz) of the total pressure measured by each of the AIP sensors in each of the circumferential rings as shown schematically in Figure 9a at $M_{AIP} = 0.5$. The bars are grouped by ring number and the data for each sensor are arranged in CW order (cf. Figure 9a). The bars shaded in gray represent missing data. The data in the absence and presence of bleed are shown in (a) and (b), respectively. Also shown are corresponding color raster plots of distributions of the time-averaged total pressure (c,e) and total pressure RMS fluctuations (d,f) at the AIP, and a power spectra for the two cases at the port marked in the spectra bars (a,b) and shown in AIP plots (c-f).*

Finally, the variations of instantaneous and time-averaged distortion and recovery over the range $0.12 \leq M_{AIP} \leq 0.6$ in the absence and presence of bleed are shown in Figure 18, where the base data from Figure 7 are repeated for reference. As discussed in connection to Figure 7, the term steady-state in this figure discussion refers to the parameter being calculated on the time-average total-pressure values, and time-average refers to the time-average of the parameter which is calculated for each instantaneous total-pressure realization. To clarify, steady-state is calculated as $X(\bar{p})$, and time-average is calculated as $\overline{X(p)}$, where X is a calculated parameter, p is the instantaneous pressures, and the bar notates a time-average.

Figure 18a shows the steady-state, time-average, and 95% confidence interval of instantaneous $DPCP_{avg}$. Perhaps not surprisingly, the steady-state distortion increases in the controlled flow, arguably due to a combination of the extremely low absolute distortion levels in the base flow and the steadying of the vortices with the bleed control. As already seen in Figure 17e, the controlled flows form distinct total pressure signatures at the AIP, which lead to the increased distortion levels. Still, the overall levels of distortion in the presence of bleed remain low in the absolute sense. The main effect of the bleed on distortion is seen as the significant lowering of the instantaneous distribution

of distortion. At most Mach numbers, the time-average distortion of the controlled flow nearly matches the bottom edge of the base flow confidence interval, corresponding to the bottom 2.5% magnitudes in the base flow. It is important to note that the time-average differs from the steady-state because of the non-linearity of the $DPCP_{avg}$ parameter ($X(\bar{p}) \neq \overline{X(p)}$), as already discussed with respect to Figure 7. At M_{AIP} = 0.5, the highest end of the base flow range, the top end of the confidence interval is reduced from above 0.35 to about 0.25. In addition, it is noticeable that the range that the confidence interval encapsulates is smaller than that of the base flow for a fixed M_{AIP}, which is another indicator of increased flow steadiness.

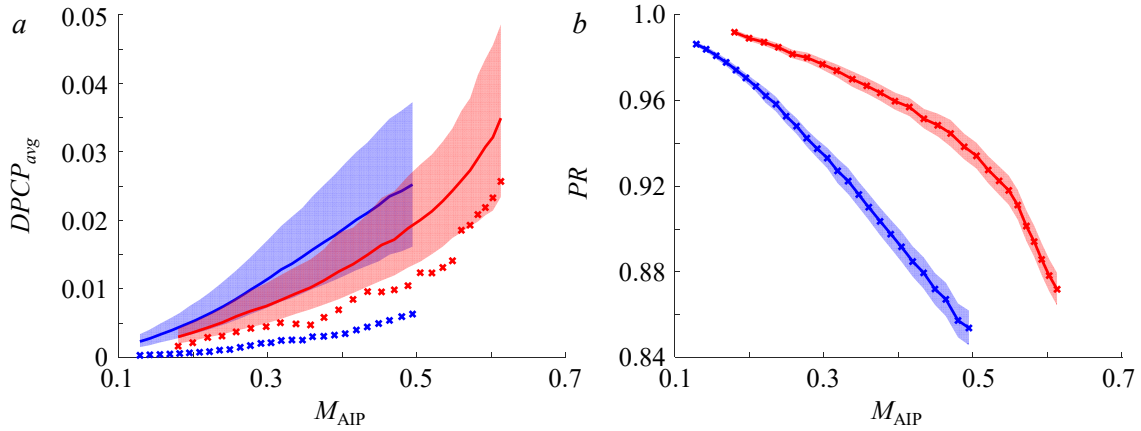

Figure 18. *Base and bleed cowl $DPCP_{avg}$ (a) and pressure recovery (b) steady state (×), time-averaged (—), and 95% confidence interval (shaded) for M_{AIP} = 0.12 - 0.6.*

The equivalent total pressure recovery variation with Mach number is shown in Figure 18b. In this case, as pressure recovery is a linear parameter ($\overline{X(p)} = X(\bar{p})$), the steady-state and time-average values coincide. As already assessed [9], there is a notable increase in the total pressure recovery across the full range of the diffuser Mach numbers. While the base flow recovery decreases in a nearly linear fashion with M_{AIP}, it is seen that the controlled flow recovery initially decreases at a lower rate with the increase in M_{AIP}, up to about M_{AIP} = 0.54. Its slope changes for the highest diffuser flow rates, and it appears that the recovery decreases thereafter at the rate comparable to the base flow. Consequently, the relative improvement in recovery is lowest at the lowest Mach numbers and then progressively increases with the increasing Mach number up to about M_{AIP} = 0.54. It should be noted that an alternative view of the achieved increase in recovery would be stated in terms of the enabled higher flow rates through the diffuser. The facility can achieve M_{AIP} = 0.6 with the bleed slots, compared to the limit of about M_{AIP} = 0.5 in the uncontrolled flow. In addition to steady-state recovery, the confidence interval shows that despite significant variation in the base flow total pressure pattern, as discussed in connection with Figure 15, the face-averaged total pressure deficit does not significantly vary in time in both the base and controlled flows.

V. Conclusions

The present experimental investigations focus on the flow through a serpentine diffuser with a cowl inlet at zero forward speed because of the known startup issues of supersonic thin-lip cowls where the drawn air separates over sharp turns into the inlet, inducing large losses and secondary vortices. The diffuser model (AIP/throat offset 0.4 D_{AIP} and L/D = 3.7) is kept the same as in earlier studies of the diffuser flow 'decoupled' from an inlet. The model is installed at the intake of an open-return, pull-down, high-speed subsonic wind tunnel and its cowl inlet is integrated with a ground plane to emulate the effect of an adjacent aerodynamic surface. As shown earlier [10], the 'decoupled' diffuser flow is governed by the local flow separation past the second turn and interaction of the corner vortices and a weak flow separation past the first diffuser turn. While the corner vortices still form about the cowl intersection with the ground plane, the flow within the diffuser with the cowl inlet is dominated by the formation and advection of a counterrotating vortex pair that forms about the center plane. In addition, the second cowl vortex merges with the initial corner vortex on each side of the diffuser, amplifying its effect and unsteadiness. The formation and downstream evolution of these vortices induce a rather dramatic loss in total pressure, resulting in up to 15% loss in recovery at the AIP.

High-frequency total pressure measurements at the AIP and stereo PIV measurements within the cowl characterize the dominant flow features and the induced unsteadiness, resulting in strong instantaneous total pressure distortion,

while, remarkably, the time-averaged circumferential distortion appears very low owing to the inherent flow unsteadiness and mixing at the AIP. Hence, the primary objective of the flow control in these diffuser flows with cowl inlets becomes focused on mitigation of the losses associated with the cowl vortices. This is proposed to be done by disrupting the formation and further interactions of these vortices and accomplished by autonomous ingestion of ambient air into the flow over the inner surface of the cowl by exploiting the inherent pressure difference across the cowl's surface through several successive narrow spanwise slots.

While the previous experimental work [9] discussed the global controlled flow features including a large increase in recovery at the highest Mach numbers, from about 0.85 to 0.93, the present study focused on the dynamic cowl flow features, as well as the measures of the flow unsteadiness at the AIP. It is shown that, past the interaction with the bleed flow through the cowl slots, both the central vortex pair and the corner vortices become progressively more deflected away from the surface and towards the bulk diffuser flow. It is interesting that both the central vortices and corner vortices become displaced by about 0.1D by the last PIV measurement plane, downward and sideways, respectively. It is argued that premature displacement of the vortices from the surface severs the vorticity supply, weakening them, and that the introduction of the small-scale vorticity from the bleed ports further promotes mixing and diffusion of the initially strong coherent structures. In addition, management of the dominant base flow features appears to revert the diffuser flow back towards the AIP structure closer to the 'decoupled' diffuser [10]. Such increased coherence of the total pressure deficit at the AIP inevitably leads to an increase in the time-averaged distortion parameter (although still small in an absolute sense), while the time-resolved peak circumferential distortion parameter $DPCP_{avg}$ is reduced by about 35% across the entire range of the present flow rates. Moreover, individual time-resolved total pressure measurements indicate that the unsteadiness is significantly reduced across all frequencies and nearly all sensors.

Acknowledgment

Support by an ONR Grant monitored by Dr. Steven Martens is gratefully acknowledged.

References

[1] Henne, P., "Low-speed test of translating lip axisymmetric inlets for subsonic transports," NASA-CR-2467, 1974.

[2] Fradenburgh, E. A., and Demarquis, D. W., "Theoretical performance characteristics of sharp-lip inlets at subsonic speeds," NACA-TR-1193, 1954.

[3] Fozard, J. W., "The Hawker P1127 vectored thrust fighter program - Lessons learned," *AIAA Paper* 90-3238-CP, 1990.

[4] Bore, C. L, "Intakes for vertical landing aircraft," *Practical Intake Aerodynamic Design*, 1993.

[5] Sóbester, A., "Tradeoffs in jet inlet design: A historical perspective," *Journal of Aircraft* Vol. 44, No. 3, 2007, pp. 705-717.

[6] Hawkins, J. E., "YF-16 inlet design and performance," *Journal of Aircraft* Vol. 13, No. 6, 1976, pp. 436-441.

[7] Powell, A. G., Welge, H. R., and Trefny, C. J., "Low-speed aerodynamic test of an axisymmetric supersonic inlet with variable cowl slot," *AIAA Paper 85-1210*, 1985.

[8] Garzon, G. A., "Use of a translating cowl on a SSBJ for improved takeoff performance," *AIAA Paper 2007-25*, 2007.

[9] Burrows, T.J., Vukasinovic, B., Glezer, A., Lakebrink, M.T., and Mani, M., "Controlled flow dynamics in a serpentine diffuser with a cowl inlet," *AIAA Paper* 2020-2951, 2020.

[10] Burrows, T.J., Vukasinovic, B., Glezer, A., Lakebrink, M.T., and Mani, M., "Experimental and numerical investigation of active flow control of a serpentine diffuser," *AIAA Journal,* Vol 59, 2021, pp. 607-620.

[11] Krishnan, A., Krishnan, A., Kearney, J., Costello, M., and Glezer, A., "Aero-driven bleed-air applied to roll control," *Journal of Aircraft*, Vol. 57, No. 4, 2020, pp. 652-663.

[12] Woodiga, S. A., and Liu, T., "Skin friction fields on delta wings," *Experiments in Fluids,* Vol. 47, No. 6, 2009, pp. 897-911.

[13] Berson, A., Michard, M., and Blanc-Benon, P., "Vortex identification and tracking in unsteady flows," *Comptes Rendus Mécanique,* Vol. 337, No. 2, 2009, pp. 61-67.

[14] Graftieaux, L., Michard, M., and Grosjean, N., "Combining PIV, POD and vortex identification algorithms for the study of unsteady turbulent swirling flows," *Measurement Science and Technology,* Vol. 12, No. 9, 2001, pp. 1422-1429.

[15] Depardon, S., Lasserre, J. J., Brizzi, L. E., and Borée, J., "Instantaneous skin-friction pattern analysis using automated critical point detection on near-wall PIV data," *Measurement Science and Technology,* Vol. 17, No. 7, 2006, pp. 1659-1669.

[16] Hyndman, R. J., "Computing and graphing highest density regions," *The American Statistician,* Vol. 50, No. 2, 1996, pp. 120-126.